Novel Polymeric-Modified PPY@GCN Based Composite for Photocatalytic Degradation of Reactive Green 5

[1]Raheeba Akbar, [1]Haq Nawaz Bhatti*, [1]Muhammad Zahid, [2]Muhammad Yasin Naz
[1]*Department of Chemistry, University of Agriculture, Faisalabad, Pakistan.*
[2]*Department of Physics, University of Agriculture, Faisalabad, Pakistan.*
hnbhatti2005@yahoo.com; haq_nawaz@uaf.edu.pk

(Received on 1st January 2025, accepted in revised form 22nd May 2025)

Summary: The widely used dye Reactive Green 5 (RG 5) endures an adverse effect on human health and water supplies, necessitating effective elimination strategies. Heterogeneous photocatalysis based on semiconductors is a sustainable approach that precisely degrades organic contaminants. The present study aims to explain and verify the effectiveness of a remarkable PPY@GCN/Bi_2WO_6 (PGB) composite for the environmental remediation of RG 5 dye. The graphite carbon nitride (GCN) based ternary composite (PGB) has been synthesized by the hydrothermal approach. The prepared composites were studied by using SEM/EDX to indicate morphological characteristics and elemental variations, XRD for crystalline arrangement, FTIR for functional groups, UV-VIS for absorption spectral data and PL for emission spectra. The characterization study assists the effective assembly of PGB composite on the surface of good crystallinity GCN nanosheets. The designed heterojunction enhances photocatalytic performance and increases the separation of photo-generated charges. Light activity on prepared composites and influencing parameters (pH, oxidant dosage, catalyst dose, initial RG 5 concentration, and irradiation time) were assessed in sunlight radiance. The appropriate conditions for photocatalytic breakdown were pH = 3, catalyst amount = 10 mg/L, oxidant dose = 10 m*M* and initial RG 5 dye concentration of 20 ppm employing a ternary PGB composite, and RG 5 dye was degraded extensively within 1 h. Under optimal conditions, the ternary PGB composite was used to accomplish 95 % degradation efficiency. The kinetic assessment indicated that experimental findings were in significant agreement with the Behnajady-Modirshahla-Ghanbery model. Reusability experiments demonstrated that catalysts may be used five times successively. Samples showed effective antibacterial properties against strains of *S. aureus* and *E. coli* and minimal cytotoxicity. A scavenging study indicated that hydroxyl radicals were the most significant reactive oxygen species involved in the photocatalytic breakdown of RG 5 dye.

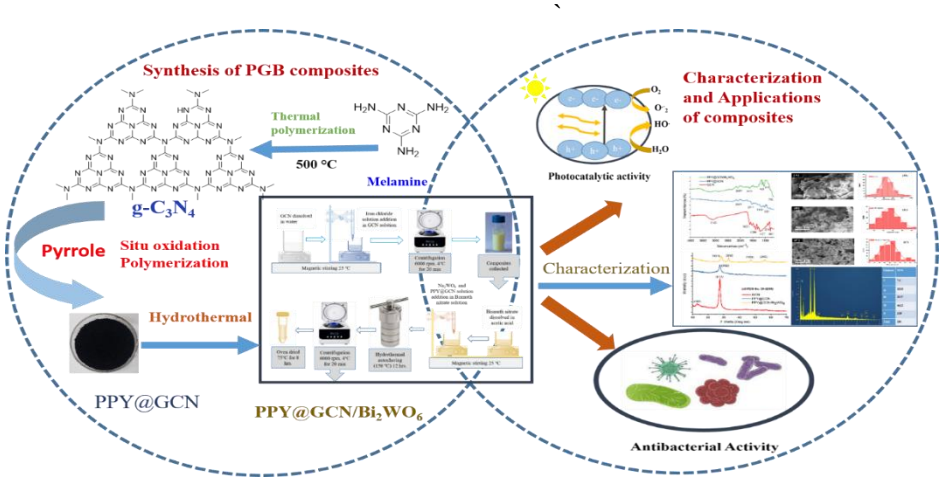

Keywords: Graphite Carbon Nitride, Bismuth tungstate, Photodegradation, Polypyrrole, Reactive Green 5, Wastewater.

Introduction

A healthy lifestyle and numerous daily pursuits, such as mining, assembling, and cultivation in agriculture, depend on preventing water pollution, which has emerged as the world's most important challenge in recent years [1]. Environmental determinants like water, vegetables, harvests, fruits, fluids, soil and numerous other variables may include organic wastewater contaminants, including synthetic

*To whom all correspondence should be addressed.

dyes, phenolic substances, food poisons, medicinal products, fungicides, herbs and pesticides, which entail devastating impacts on both the surrounding environment and living things [2]. Their discharge into reservoirs substantially decreases the quality of the ground and surface waters, posing serious health risks to all aquatic creatures and exacerbating existing socioeconomic concerns. Through their sluggish biodegradation, long-range transport attributes, and elevated chemical stability, they accumulate in living tissues and perturb the food chain [3]. The most commonly encountered pollutants released into aquatic regions are presumed to be dyes, due to their prospective applications in numerous sectors, including the food, plastic, textile, precious stone, cosmetic, and paper industries [4]. By obstructing the ingress of solar light and lowering the concentration of dissolved oxygen (DO), the presence of such obscure aromatic organic substances in an aquatic environment prevents the development of marine biota. The most recent estimate is that the global production of synthetic dyes is around seventy thousand tons annually, leading to a significant volume of wastewater [5].

Azo dyes are the major family used in textiles, encompassing between 60 and 70 per cent of all textile dyestuffs used [6]. They are characterized by having at least one azo bond (-N=N-) in their composition, and Reactive dyes are classified as azo dyes. Reactive dyes' intricate structure and non-biodegradable characteristics make them stubborn materials that could be hazardous to the environment and human health [7]. As depicted in Fig. 1, RG 5, also known as Procion Green H4G, is a member of the triazine dye family and has three secondary amino groups, seven sulfonate groups, and a Cu (II)-bonded phthalocyanine (PC) moiety in its molecular structure. RG 5 harms humans and the environment [8]. The specific formulation of RG 5, along with its coloring abilities, soluble content, durability, lifespan, hypoallergenic properties, and harmful attributes, allows for a vast array of uses [9]. The dye is frequently utilized in the food processing sector as agents against fungi and bacteria, in addition to serving as colorants for materials such as wool, silk, cotton, paper products, pulp, and leather [10]. Its harmful potential grows with elevated temperatures, prolonged contact, and higher concentrations [11]. It may cause vomiting, an elevated heartbeat, cyanosis, jaundice, and tissue necrosis, among other negative consequences [12]. Therefore, it is essential to properly treat wastewater polluted with RG 5 before discharging it into freshwater sources for environmental purification.

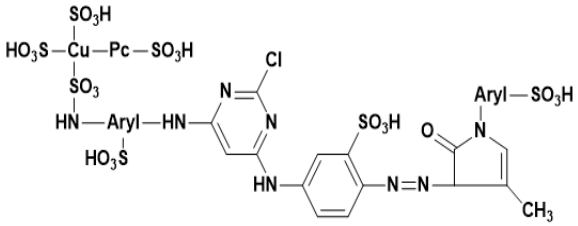

Fig. 1: Structure of Reactive Green 5 dye.

Traditionally, several wastewater treatment techniques, including membrane filtration [13], adsorption [14], and biodegradation, are available to break down pollutants in wastewater. Although all these methods are important for cleaning up contaminants in water, they have certain disadvantages, such as being expensive, requiring significant time and effort, needing skilled labor, and providing only partial removal of toxic ingredients by shifting toxins from the liquid state to solid form, which results in the production of recirculating sludge [15]. Among the most effective strategies for the oxidative breakdown of organic contaminants are advanced oxidation processes (AOPs) [16]. Due to their strong mineralization potential, AOPs are highly appealing for practical applications, generally arising from the production of reactive oxygen species (ROS) such as •OH, •HO_2, and •O_2^-. Hydroxyl radicals, which are highly reactive species generated in situ in AOPs, cause organic pollutants to oxidize non-selectively to H_2O, CO_2, and specific inorganic ions [17]. One of the most promising AOPs is semiconductor-based heterogeneous photocatalysis, which is regarded as an exceptional renewable energy conversion process effective in pollutant removal at room temperature and pressure.

GCN, a semiconductor in the form of a metal-free 2D polymer, has garnered significant interest because of its remarkable intrinsic characteristics, including affordability, easy synthesis, adjusTable electronic properties, appropriate band gap, high abundance of elements, environmentally friendly nature, and excellent thermal and chemical stability [18]. GCN has been widely investigated for its ability to degrade stubborn pollutants under visible light, attributed to its intermediate bandgap between 2.4 and 2.7 eV. However, the photoactivity of GCN is restricted by the rapid recombination rate of the photoinduced e^-/h^+ pairs [19]. Several GCN-based heterojunctions, such as g-C_3N_4/$SnFe_2O_4$ [20], g-C_3N_4/Ag@$CoWO_4$ [21], Pt/g-C_3N_4 /$SrTiO_3$ [22], g-C_3N_4/Carbon nanotubes/WO_3 [23], g-C_3N_4/Mo@WO_3 [24] and Zn/Ag/g-C_3N_4 [25], have been documented to show significantly enhanced photocatalytic

performance, leading to a reduction in the rate of e^-/h^+ pairsBi_2WO_6, known as (BWO), has garnered significant interest lately as a remarkable photocatalyst for visible light, owing to its corner-sharing arrangement of WO_6 octahedral situated between $(Bi_2O_2)^{2+}$ layers [26]. However, GCN and BWO incorporate sequential band gaps and appropriate points for the conduction band (CB) and valence band (VB), which are essential to photocatalysis [27]. The GCN/BWO heterojunction nanocomposite has demonstrated remarkable performance, leading to improved photodegradation of the compounds. Recently GokulaKrishnan *et al* developed g-C_3N_4/Bi_2WO_6 hetero structures for the photodegradation of pirimicarb at pH 5 [28]. Deng *et al* Designed Ag@CNG composites for the photodegradation of dimethoate under visible light [29]. The recycling and separation of catalysts is crucial for their application in wastewater treatment. However, given the apprehensions surrounding nanotoxicity and the difficulties associated with the composite's strength, charge transfer and recoverability, this study proposes a significant and uniform amendment of the GCN/BWO composite using a conductive polymer.

Recently, amending (GCN/BWO) with a conductive polymer to improve mechanical strength, stability, and biocompatibility is an effective strategy to increase its use in energy storage or photocatalysis. However, polypyrrole (PPY) is a conducting polymer known for its durability, excellent electrical conductivity, and reliability in various environmental conditions [30]. It serves as an h^+ transporter and an electron donor when exposed to visible light, leading to its use in photocatalysis, detection devices, corrosion mitigation, and organic solar power cells. PPY can absorb ions because of the positively charged nitrogen atoms within its polymer framework [31]. It has been noted that merging PPY with various semiconductor materials improves the elimination of pollutants via ion interchange or electrostatic interactions. Using the PGB composite makes photocatalytic degradation 2 to 2.9 times more efficient than implementing GCN or PPY@GCN individually.

In the present study, we report the PGB ternary composite, where GCN/BWO were employed as photocatalysts and PPY as h^+ transporter and electron donor. The in situ hydrothermal technique was employed to create a new PGB composite, which was then used to degrade RG 5 dye under sunlight. The photocatalytic activity of PGB, composed of the BWO and Polypyrrole-based GCN, on RG 5 degradation has not been reported.

Experimental

Materials and reagents

Bismuth nitrate pentahydrate ($BiNO_3.5H_2O$, 97 %), sodium tungstate dihydrate ($Na_2WO_4.2H_2O$, 98 %), sodium hydroxide pellets (NaOH, 96%), and pyrrole were supplied from Sigma Aldrich- USA. Pure melamine powder ($C_3H_6N_6$, 98.6 %) was taken from Scharlau Spain. Hydrogen peroxide (H_2O_2) was procured from UNI-CHEM reagents. Analytical standard ethanol (C_2H_5OH, 95.5 %) was obtained from Merck, Germany. Anionic dye RG 5, which was acquired from Fischer Scientific, was used as a model pollutant for the assessment of photodegradation. Although all the chemicals and reagents used in the process of formation were high-purity analytical quality, no further purification was mandatory. Double-distilled water was collected from a water distiller instrument and used to prepare reaction solutions for the duration of the research project.

Synthesis of graphitic carbon nitride (g-C_3N_4)

g-C_3N_4 was synthesized using a thermal polymerization method [32]. A pristine alumina crucible was filled with 10 g of melamine and sealed with a cover. It was heated for four h at 550 °C (continuous heating rate 4 °C min^{-1}) in a muffle furnace to produce a yellow solid by thermal polymerization [21]. The acquired yellowish-white fine powder was left to cool down without further decontamination. Fig. 2 illustrates a structural modification that occurs when melamine is used to synthesize GCN.

Synthesis of PPY@g-C_3N_4 composite

The polypyrrole-based binary composite was synthesized via in situ oxidation polymerization approach. First, 0.4 g of GCN was added to 40 ml of deionized water using a sonication process. The oxidizing agent (0.5 *M* of $FeCl_3$) is immersed in 100 ml of deionized water and subsequently incorporated into the solution of dissipated composite, followed by thorough mixing with a persistent stirring. After that 3 *M* of pyrrole monomer was added to the prior solution, and the oxidation reaction occurred. The prepared solution was left overnight, filtered, and rinsed with ethanol or purified water to eliminate monomers. The composites were dried in an oven at 60-70 °C and stored in air-tight bags for future use.

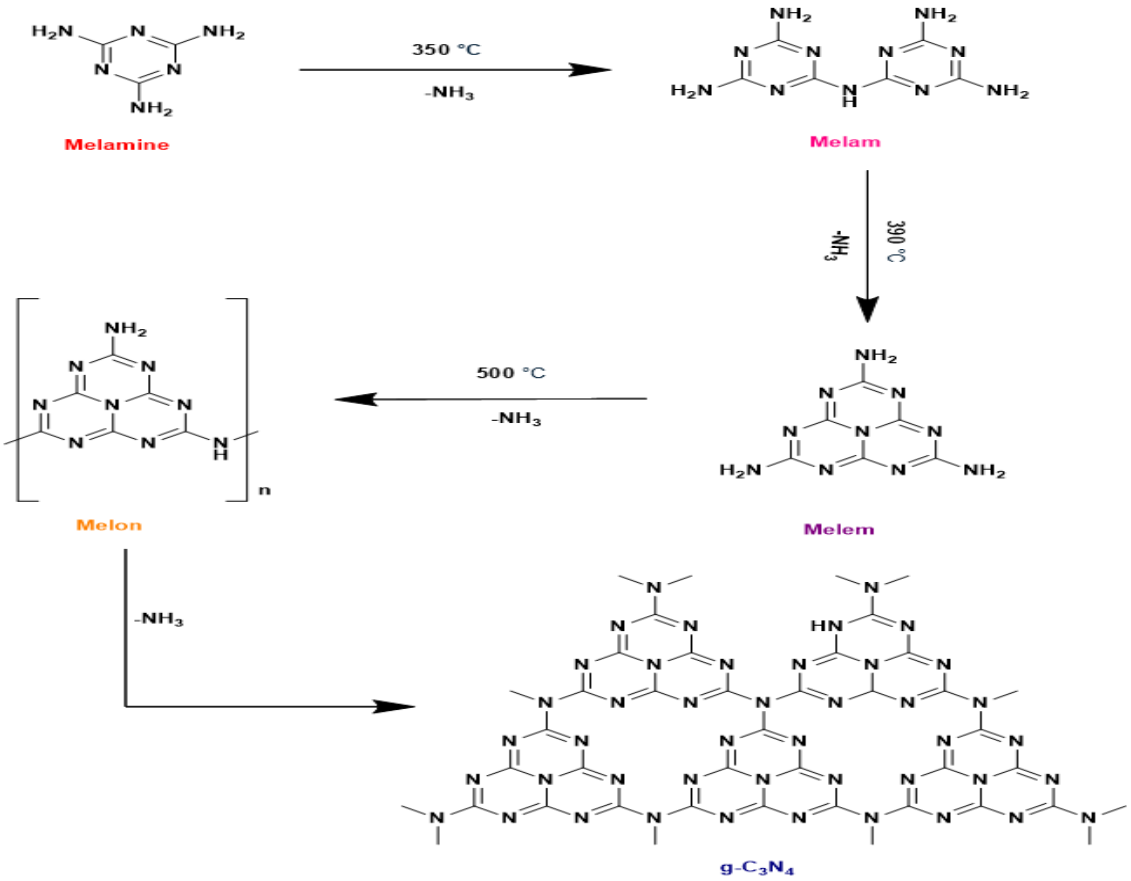

Fig. 2: Reaction pathway for the synthesis of g-C_3N_4.

Preparation of PPY@g-C_3N_4/Bi_2WO_6 composite

The heterojunction photocatalyst of PGB was synthesized using a hydrothermal method. Firstly, 5 mmol Bi $(NO_3)_3.5H_2O$ was dissolved in 40 ml of glacial acetic acid under constant stirring. In the meantime, 2.5 mmol $Na_2WO_4.2H_2O$ and a sufficient amount of polypyrrole-based Carbon nitride were dispersed into 20 ml of distilled water. The suspension, as mentioned above, was mixed aggressively for 30 min, meanwhile, the Bi $(NO_3)_3.5H_2O$ solution was added dropwise. The resulting solution was then put into an autoclave coated with Teflon and heated to 180 °C for 12 hrs. Ultimately, the product was obtained by centrifugation and dried for 10 hrs at 80 °C. A schematic illustration of the synthesis procedure is presented in Fig. 3.

Characterization techniques

The as-synthesized GCN-based composites were analyzed through various characterization techniques. The photocatalyst's morphological characteristics and elemental variations were investigated by using a scanning electron microscope (SEM, Quanta 250 FEG) and an energy-dispersive X-ray spectrometer (EDS). The finished product was dispersed using the sonication process in an ethanol solution to provide materials for the SEM assessment. To construct a sTable sheet for monitoring, the mixture was then applied to copper grids covered with carbon. The crystalline arrangement and purity of the phases in the prepared materials were investigated by an X-ray diffraction (XRD) instrument (X' Pert PRO diffractometer) with a Cu/Kα radiating source, functioning in the 10–90° range of the scanning angle 2θ at a rate of 2°/min. The specific functional groups of the prepared composites were identified using Fourier transform infrared spectroscopy (Agilent Cary 630 FT-IR) within a wavenumber range of 650-4000 cm^{-1}. The ophthalmic characteristics of the prepared materials were evaluated using UV–Visible spectroscopy. UV-visible absorption spectral data were obtained using a (CE Cecil 7200) spectrophotometer, which functioned within a wavelength assortment of 200–800 nm by dissolving the prepared materials in a solution of ethanol and then sonicating them for 20 minutes. The bandwidth energy of the constructed heterostructures was obtained from the optical absorption spectra using the Tauc Equation. Photoluminescence

(PL) spectra were performed on an (RF5301) spectrophotometer with an excited wavelength range of 335 nm as well as a scanning wavelength range of 400–700 nm.

Photodegradation experiments

The prepared photocatalyst's efficacy was evaluated by removing RG5 dye under visible light irradiation. The impact of different parameters, e.g. pH (2–9), composite dose (5–25 mg), Dye concentration (10-50 ppm), and contact duration (10–120 min) was perceived. In the current study, RG 5 was taken as a model pollutant. With the help of a pH meter, 2 *M* concentration of sodium hydroxide and Hydrochloric acid were used to adjust the pH of the RG 5 dye solution. After dispersing the required quantity of photocatalysts in a 20 ppm RG 5 dye having 100 ml of solution, the mixture was sonicated for a period of approximately two to three minutes. Subsequently, a certain concentration of H_2O_2 was introduced into the reaction mixture. In a standard investigation, 10 mg of the offered catalyst was amalgamated with 60 ml of a 10 mg/L RG 5 dye solution and magnetically stirred in the dark conditions for approximately 30 minutes to accomplish adsorption or desorption equilibria of the dye on the synthesized surface of the catalysts before exposure to sunlight. Then RG 5 solution was set in an electrical orbital shaker and run at 150 rpm for one hour in the presence of sunlight. A composite was extracted from the RG 5 solution via centrifugation, and absorbance was identified at 660 nm using a UV-visible spectrophotometer. The extent of dye degradation was assessed by comparing the absorbance of the treated and untreated RG 5 dye solutions. The extent of degradation of the dye was calculated by using the formula specified in Eq. (1)

$$\%\ Degradation = 1 - \frac{A}{A_o} \times 100 \qquad (1)$$

Here, initial absorbance is referred to as Ao, while absorbance adhering to degradation in the presence of sunlight is represented by A.

Evaluation of antibacterial efficacy

The antibacterial efficacy of prepared composites was assessed qualitatively according to the (ATCC-25922) ordinary test method, testing contrary to the strains of bacteria *Escherichia coli* and *Staphylococcus aureus*, adopting the agar-well diffusion method. In a standard process, (5×10^5 CFU/ml) of every cultivar of bacteria was applied to the surface of the agar plate. The petri dish containing the inoculation was filled with agar and carefully stirred. After solidification, agar wells with 6 and 8 mm diameters were carefully created using hygienic Pasteur pipette tips. Subsequently, the agar plates were cooled only for 40 minutes to allow the antimicrobial agent to spread evenly through the agar medium, preventing the development of the specific bacterial strain. Plates made of agar were kept in an incubator at an appropriate temperature of (37◦ ± 1 ◦C) for just 18 h, and the sizes of the inhibitory zones were recorded in millimeters (mm).

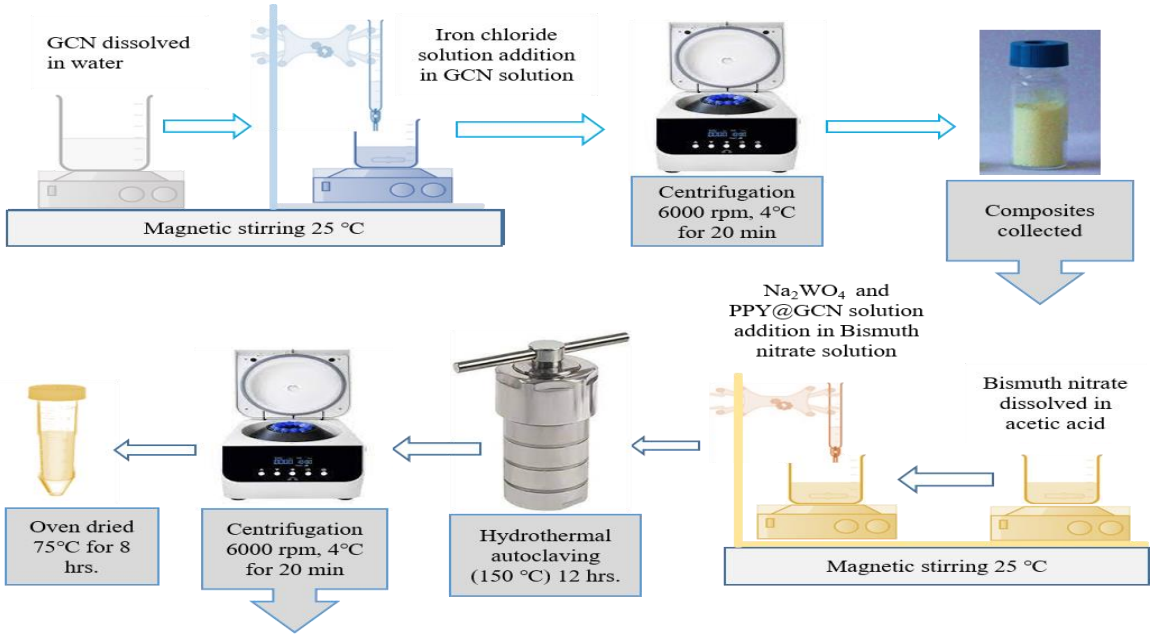

Fig. 3: A schematic representation of the synthesis of PPY@GCN/Bi_2WO_6 composite.

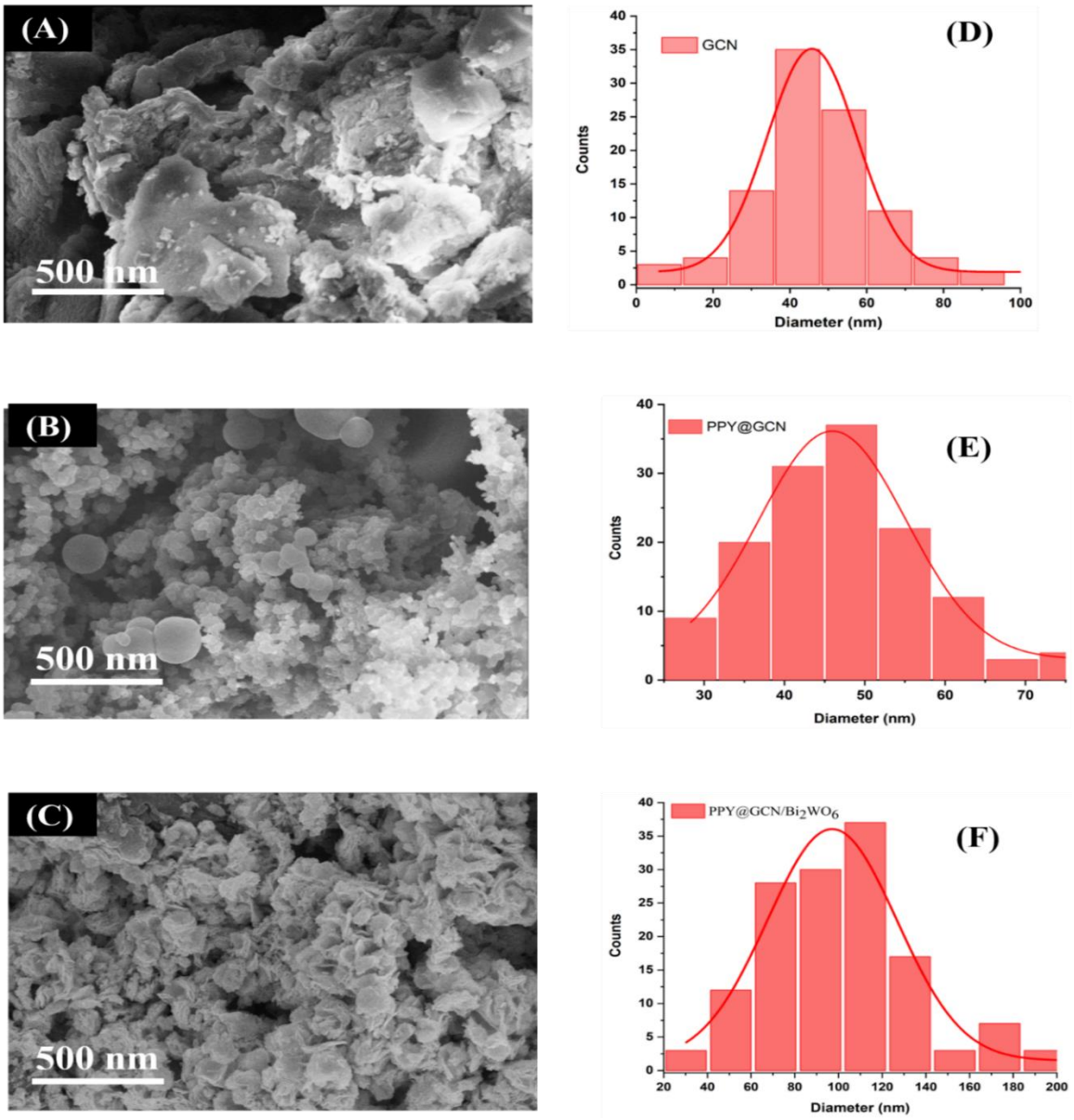

Fig. 4: SEM images, (A) GCN, (B) PPY@GCN, (C) PPY@GCN/Bi_2WO_6, Composites with corresponding histograms (D) GCN, (E) PPY@GCN, (F) PPY@GCN/Bi_2WO_6.

Results and Discussion

Scanning electron microscope

The structure of the surface significantly influences the chemical processes taking place on the surface [33]. SEM and histograms noticed the morphologies of GCN, PPY@GCN, and PGB composites, as shown in Fig. 4 the morphology of unaltered GCN exhibits a layered structure shown in Fig. 4(A) PPY was extensively distributed and anchored onto GCN nanosheets, which displayed cavities occupied by layers of thin lamellar structures that formed large, irregular voids, leading to uneven spongy particles shown in Fig 4(B). The image of PGB Fig.4 (C) displayed a two-dimensional structural form consisting of stacked sheets with wrinkles and an irregular shape characteristic of typical hierarchical structures, attributed to the effective aggregation of BWO onto PPY@GCN. Further, SEM images were analyzed to determine the standard particle size and the role of the composites. The ordinary granule size of the GCN nanosheets was assessed to be 35 nm based on 100 measurements, of which 35 were found to be in the 25–45 nm range Fig. 4(D)**.** In contrast, polymer-based graphitic carbon nitride-based composite Fig. 4(E) demonstrated an average size of particles 45 nm,

constructed on 140 observations, with 40 falling within the range of 39-51 nm. However, based on 124 observations, the typical size of the PGB composite was estimated to be 105 nm, with 35 of those measurements placed between 90-120 nm ranges Fig. 4(F). The elemental mapping indicated that the primary components of the composites were C, N, O, W, and Bi, with percentage compositions of 7.4, 3.99, 15.03, 29.37, and 44.21, respectively Fig. 5. The presence of BWO on the PPY@GCN sheet suggests that the produced heterojunction composites are free from impurities, and the XRD results further support this.

Fig. 5: EDX spectra of PGB composite.

X-ray diffraction (XRD) analysis

XRD analysis was employed to assess the phase purity, conduct a structural examination, and evaluate the crystallinity of the GCN-based composites. The XRD conFiguration shown in Fig.6 evaluated the crystal structure of GCN, PPY@GCN, and the novel ternary PGB composites. The more intense peak observed at 27.3° is linked to the interlayer stacking designated as (002). In comparison, the peak at 13.1° is related to the in-planar repeating unit, consistent with the standard pattern [34]. The significant stacking density is due to the powerful π-π interaction among the carbon and nitrogen atoms categorized in the triazine structures [35]. The XRD conFiguration of PPY@GCN indicates a diminution in peak intensity of the GCN structure, and an additional diminutive bump at 24.6° signified the effective formation of PPY@GCN. Four distinctive peaks ought to be observed in the XRD pattern of the PGB composite at 28.5°, 33.1°, 47.2°, and 55.7°. These correspond to the orthorhombic phase BWO planes (0 0 2), (2 0 2), (1 3 3), and (2 6 2). When the binary and ternary composites based on BWO were introduced, the XRD pattern predominantly revealed the characteristic peaks of BWO due to its substantially higher diffraction intensity compared to PPY and GCN. XRD of the prepared novel PGW composite showed peaks attribuTable to GCN, PPY@GCN and PGB, illustrating the effective preparation of the ternary composite. In the PGB composite, no significant diffraction peaks of any impurities were observed, signifying that the assembled composite is pure. The average size of particles was computed using the Debye-Scherrer formula.

$$D = \frac{K\lambda}{\beta COS\theta} \qquad (2)$$

The Scherrer constant is valued at 0.94, with lambda (λ) representing the wavelength of the X-ray source (specifically, 0.154 nm). D represents the extent of the crystallite. The size parameter pertains to the dimensions, while β denotes the full width at half maximum of the PGB plane, and Θ indicates the angle of diffraction. The crystallite dimensions (D) for GCN were determined to be 5.93 nm, while for, it was PPY@GCN and PGB calculated as 9.08, 15.17 nm.

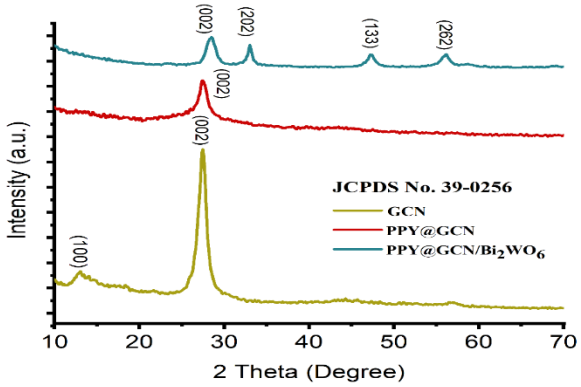

Fig. 6: XRD analysis of GCN, PPY@GCN and PPY@GCN/Bi_2WO_6.

FTIR analysis

FTIR spectroscopy was utilized to evaluate the surface composition and functional group existence. The outcomes are illustrated in Fig. 7**,** the FTIR spectra of pure GCN, the broad regions from 3000 to 3400 cm^{-1} are indicative of the (N–H) Vibration [36]. The presence of GCN is confirmed by the vibrations caused by stretching of (C–N) and (C=N), which correspond to the band peaks between 1060 and 1600 cm^{-1} [37]. The peak levels at 802-876 cm^{-1} are attributed to the indicative bending resonance of the triazine ring [38]. Further, the chemical structure of the polymer-treated GCN confirmed an absorption region at 2087 cm^{-1} associated with the (N—C—N) group and an adjacent band at 1544 cm^{-1} for (N–H) bending while the (C–N) absorption spectrum is discernible at 1031-1166 cm^{-1}, representing the prolifically coupled material in the form of composite. In the FT-IR spectra of ternary composites, the absorptions at 702-875 cm^{-1} correspond to (W=O) and (Bi=O) stretching modes, respectively. The PGB composite showed all these absorption bands, revealing the effective assembly of the heterojunction.

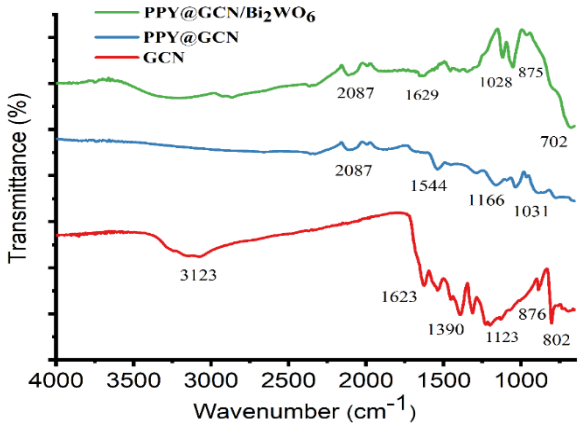

Fig. 7: FTIR spectra of GCN, PPY@GCN, and PPY@GCN/Bi_2WO_6.

Optical analysis

The UV/Vis reflective spectrum of the prepared samples is recorded to investigate the visual characteristics of the synthesized composites compared to the pure Pristine GCN and PPY-based GCN. The interaction between light waves and polymer-based composites leads to the oscillation of electrons, which is a key factor for producing surface plasmon resonance (SPR) [39]. The UV-Vis absorption procedure is influenced by structural features and the hydrodynamic environment of colloidal suspensions and their interactions with composites. In addition to the structural characteristics, the UV–vis absorption phenomenon is dependent on the hydrodynamic cloud present in colloidal suspensions and the interactions involving composites. This phenomenon, in turn, influences the surface behavior of composites [40]. The absorbance spectra of the prepared materials are within the visible range (400–800 nm), indicating the novel PGB photocatalyst's capability to respond to visible light. The absorbance spectra of GCN revealed an absorption spike at a maximum wavelength of 403 nm, which can be attributed to the excitation of surface-plasmon resonances in the 2D structures of GCN. This phenomenon accounts for the yellow coloration observed in colloidal dispersions, see Fig. 8 (GCN). With the incorporation of PPY into GCN, the corresponding peak was relocated to 433 nm, which is illustrated in Fig. 8 (PPY@GCN). It is important to note that adding PPY to GCN enhances charge transfer capabilities and boosts the mechanical strength of the composites. The corresponding peak was also displaced to 461 nm in the polymer-treated bismuth-based PPY@GCN/BWO heterostructures, as illustrated in Fig. 8 (PPY@GCN/Bi_2WO_6). This increase in peak shift could be linked to the enhancement of porosity following bismuth treatment. Therefore, porous substances with a greater specific surface area might accommodate extra oxygen vacancies, reducing the bandgap. For further study, the calculation of the bandgap energy for PGB exploited Tauc's equation based on the UV/Vis absorption ends, as represented in Eq. (3)

$$(\alpha h\nu) = k\,(h\nu - Eg) \qquad (3)$$

Specifically, "α" represents the index of absorption coefficient, "h" stands for Planck's constant, "v" denotes the frequency of the incoming photon, "K" for an energy-independent constant, "Eg" for the energy bandwidth, and "n" for the kind of transition taking place in the semiconductor. For direct semiconductors, n is equal to 2. The bandwidth was determined from the plot of $(\alpha hv)^2$ against Energy (eV). The energy band gap of GCN is reported as 2.74 eV [21]. Polymer-treated bismuth tungstate-based heterostructures reduce the energy bandwidth to 2.49 eV, as shown in Fig.8 (B). The energy bandwidth of the ternary composite, PGB, was recorded as 2.35 eV. This indicated that the separation of photogenerated pairs of electrons and holes (e^-/h^+) in PGB would improve and be more efficient under sunlight, thereby enhancing photocatalytic performance.

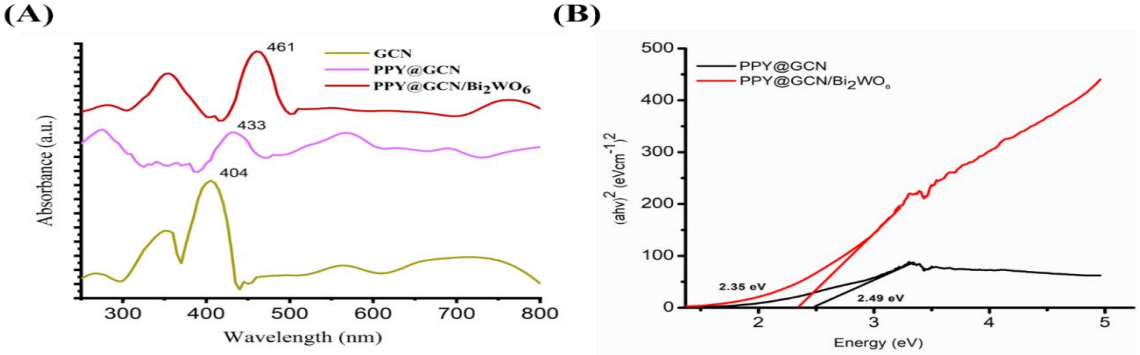

Fig. 8: (A) UV-vis spectra (B) bandgap energy of GCN, PPY@GCN, and PPY@GCN/Bi_2WO_6

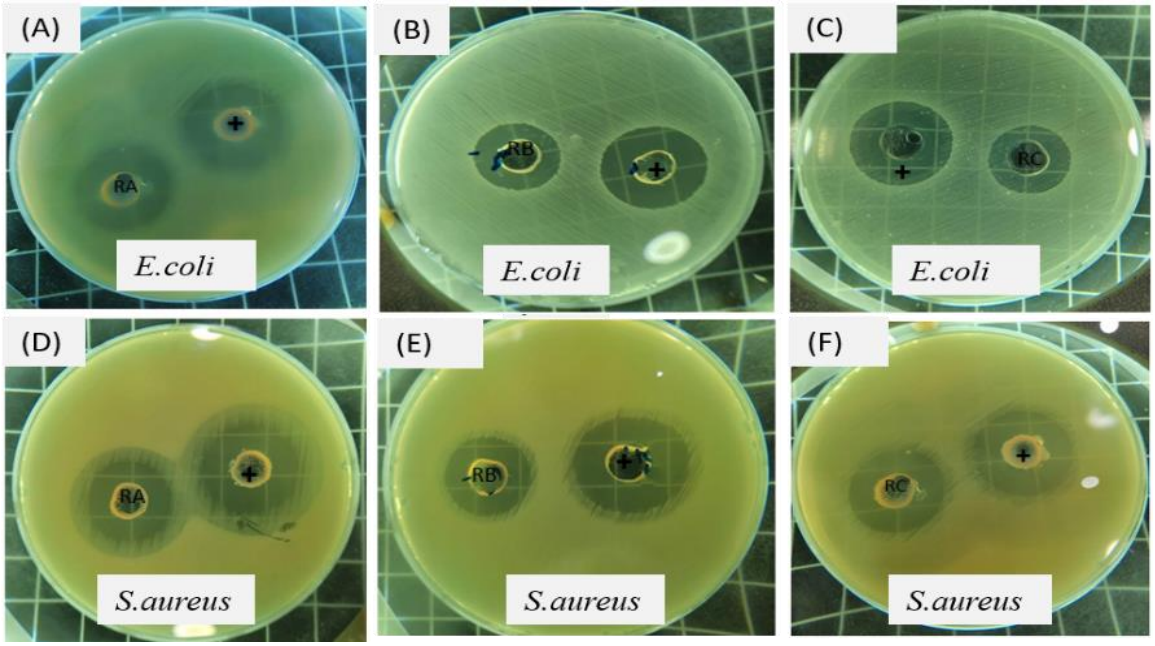

Fig. 9: Antibacterial activity of GCN against (A) *E.coli* (D) *S.aureus*; PPY@GCN against (B) *E.coli* (E) *S.aureus*; PPY@GCN/Bi_2WO_6 against (C) *E.coli* (F) *S.aureus*.

Anti-bacterial analysis

The antibacterial efficacy of GCN, PPY@GCN, and PGB composites against gram-positive (G+) and gram-negative (G-) bacteria was evaluated in addition to the photodegradation capabilities for various organic effluents. *E. coli* and *S. aureus* were utilized as G+ and G- bacterial strains to conduct disc diffusion experiments at 100 microgram concentrations to observe the antibacterial activity. The results are illustrated in Fig. 9. The suppression of bacterial growth was observed to rely on the dimensions of the inhibition zones. A relatively extensive inhibition zone indicates a more effective action against pathogens due to the interaction of the synthesized compounds, while a narrower inhibition zone signifies a lower antibacterial efficacy [41]. The pristine GCN exhibited an inhibition zone of 8 mm for *E.coli* and 10 mm for *S.aureus* (Fig. 9A-D), while polymer treated composite indicated a wider inhibitory region of 12 and 15 mm (Fig. 9B-E), whereas the PGB composite depicted a still lower inhibition zone (7-9 mm) as compared to a GCN or polymer treated GCN (Fig. 9C-F), against *E. coli* and *S. aureus*, respectively. Minimal inhibition zones for microbial growth were observed in PGB composites, shown in Fig. 9 (C-F). The superior performance of the PPY@GCN composite can be attributed to the extensive surface area provided by the sample and the enhanced photo-responsive characteristics stemming from the synergistic interaction between PPY@GCN and GCN. The main primary charge carriers engage with molecular oxygen and water (H_2O) to generate active free radicals known as ROS, specifically ($^{\bullet}O_2$) and ($HO^{\bullet}$) [42]. These free radicals directly attack bacterial cells and break apart their cell membranes. As a consequence, K+ triggers the bacterial cell to release its cellular matrix, which destroys the bacterium [43]. In addition, (ROS) engage directly with the DNA and ribosomes of bacterial cells, breaking them down into their basic elements. A lack of K+ in cells disrupts critical cellular functions such as respiration and division, leading to inhibited growth and the eventual death of bacterial cells [44].

Photoluminescence study

The efficiency of electron-hole recombination in the synthesized photocatalysts was examined utilizing the photoluminescence (PL) spectroscopic technique. In PL analysis, the sample is initially stimulated optically in its pristine state, and subsequently, the energetic electrons return to their ground state, causing radiative relaxation to occur. Oxygen vacancies, Optical properties of photocatalyst, surface states, band positions, and self-trapped exciton primarily determine PL emission [45]. PL spectra for GCN and polymer-treated PPY@GCN and PGB composite were collected at room temperature with an excitation wavelength of 800 nm. In the hypothesis, the effectiveness of separating photogenerated electron-hole pairs is assessed by the intensity of PL. Fig. 10 displays the PL emission spectra for both GCN and GCN-based polymer composite, which indicates that pristine and its composites displayed

inherent emission peaks spanning from 300 to 640 nm, but the highest PL intensity occurred at approximately 590–640 nm. After hybridization, the PPY@GCN/Bi_2WO_6 composite showed decreased photoluminescence emissions relative to both GCN and PPY@GCN, suggesting that the creation of the composite successfully diminished the rate of electron and hole recombination. As a result, when compared to the other photocatalysts, it is predicted that the PPY@GCN/Bi_2WO_6 photocatalyst demonstrates superior photocatalytic efficiency. This will be verified later in the context of the photocatalytic investigation regarding the degradation of RG 5. These outcomes were in close agreement with those reported by [46].

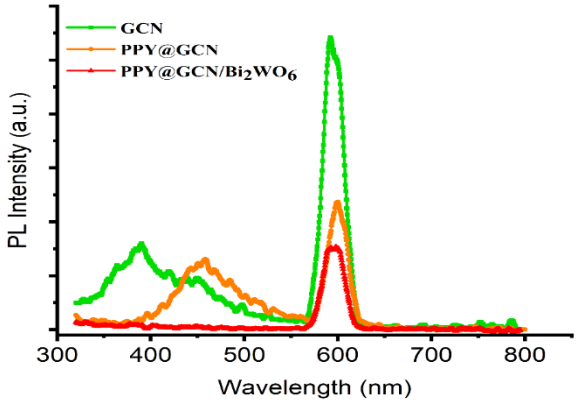

Fig. 10: Photoluminescence spectra of GCN, PPY@GCN and PPY@GCN/Bi_2WO_6.

Impact of various parameters on photocatalytic activity

Effect of pH and point of zero charge

The effectiveness of the PGB composite in photocatalysis was assessed across various pH levels (ranging from 2 to 9), and the results were collected after different time intervals. The photodegradation of RG 5 dye has been investigated, as depicted in Fig. 11 (A). The experimental findings show that dye degradation was highly effective in acidic environments. The maximal photodegradation of RG 5 using GCN, PPY@GCN, and PPY@GCN/Bi_2WO_6 composites was achieved at pH 3; with a gradual increase in pH values, the dye degradation decreases, making the optimized pH 3. The high degradation at acidic pH is due to the interaction of the anionic dye RG 5 with the positive catalyst surface [42]. The positively charged surface in acidic environments facilitates dye adsorption, leading to improved dye breakdown in sunlight [43]. The pH of the solution influenced the surface characteristics of the photocatalysts in RG 5 photodegradation. The efficiency of RG 5 degradation using the GCN composite was 95 % at pH 3 within one hour. The rate of solution degradation decreases as its pH rises. This might be due to Fenton's reagent producing hydroxyl radicals at low pH levels, which are the most active ROS for dye photodegradation [44]. The calculated pHpzc of GCN, PPY@GCN, and PGB was 6.0, 7.12, and 7.23, respectively. The pHpzc of GCN and its composites is illustrated in Fig. 11(B). This results in good agreement that GCN and its composites indicate optimal activity at a pH lower than the photocatalyst's pHpzc. The lower pH value than pHpzc charges the composite's surface positively, encouraging RG 5 (anionic dye) adsorption, which leads to enhanced adsorption and increased photodegradation [45]. The GCN-based composite showed 81% and 95% degradation at pH 3 in the presence of sunlight under optimized conditions.

Effect of catalyst concentration

The assessment of material efficacy and cost both depend on the optimization of solid content. Therefore, the GCN, PPY@GCN, and PGB concentrations were adjusted by identifying the range of 5–25 mg in 100 ml RG 5 solution under appropriate pH. The outcomes of catalyst dosage optimization are illustrated in Fig. 11(C). The results showed that the dose of the photocatalyst had a significant impact on the degradation of RG 5. The Photodegradation ability of GCN was improved from 81 to 95% as the composite dosage was increased from 5 to 10 mg. The reason is that more active sites were available, leading H_2O_2 to be catalyzed down more quickly and producing more hydroxyl radicals [47]. However, when the composite dosage was increased to 20 mg, the degradation efficacy reduced modestly from 95 to 90% and substantially below 20 mg. This might be explained by the obstruction's effect brought around by higher concentration Fe ions in heterogeneous photo Fenton strategies that serve as foragers, as shown in Eq.4. Moreover, a higher quantity of the catalyst would increase process turbidity and reduce the amount of sunlight required for Fe^{3+} photo reduction in Eq. 5 [48]. Furthermore, Fe^{2+} will react with OH^- to form $Fe(OH)_2$ (sludge), as illustrated in Eq. 6.

$$Fe^{2+} + OH^{\cdot} \rightarrow Fe^{3+} + OH^- \quad (4)$$

$$Fe^{3+} + sunlight\ (hv) \rightarrow Fe^{2+} \quad (5)$$

$$Fe^{2+} + 2OH^- \rightarrow Fe(OH)_2 \quad (6)$$

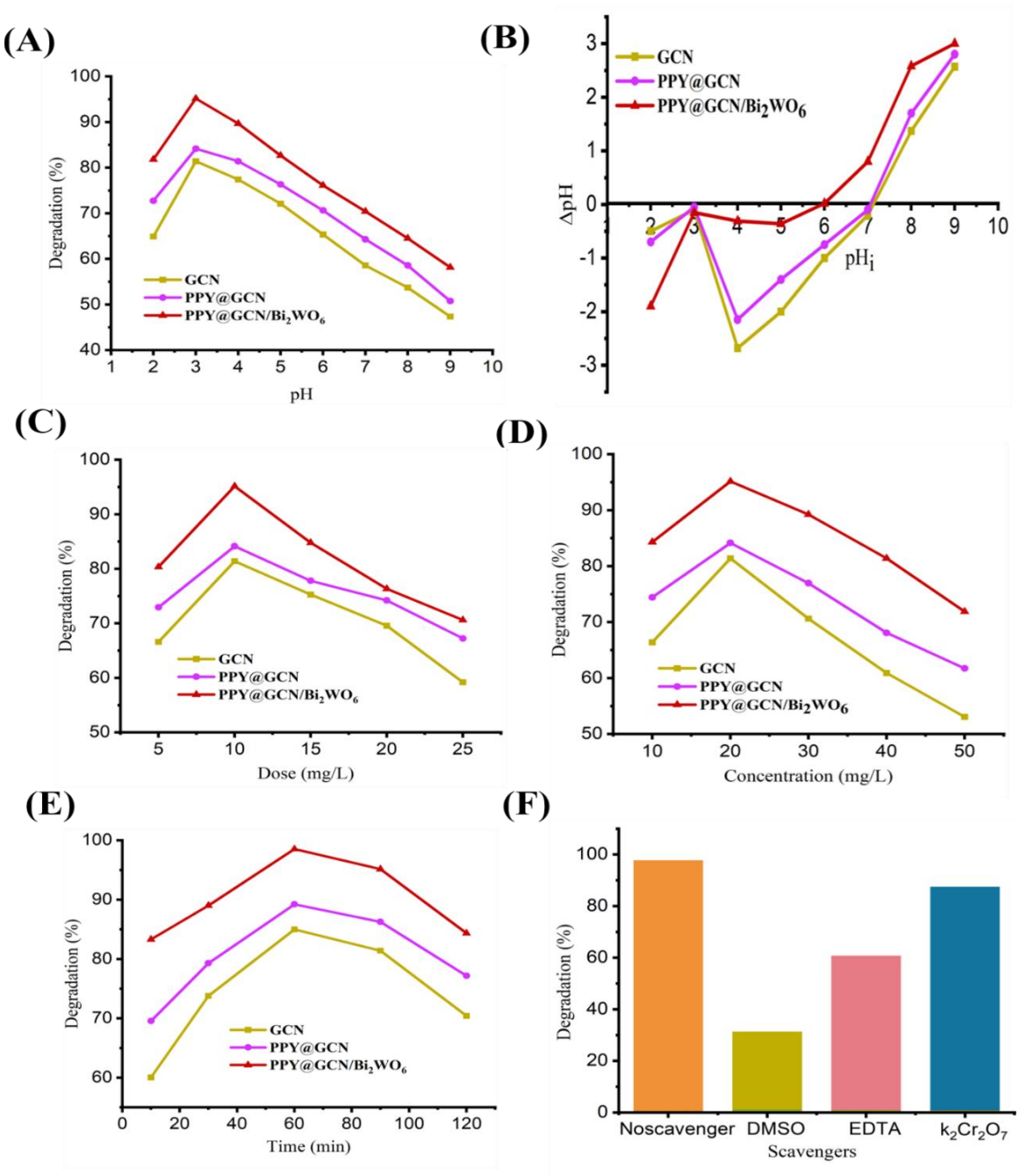

Fig. 11: Factors affecting the RG 5dye photodegradation rate of GCN-based composites (A) pH, (B) Point of zero charges, (C) composite amount, (D) initial dye concentration, (E) time, and (F) radical scavengers experiment.

Effect of dye concentration

Dye degradation efficacy depends on its nature, concentration, and presence of other molecules in an aqueous medium [49]. The degradation efficiency of RG 5 was examined by changing the RG 5 dye dose from 10 to 50 ppm for GCN, PPY@GCN, and PGB composites, keeping all other parameters constant Fig.11(D). The degradation process increased rapidly at initial RG-5 concentrations, respectively. When RG 5 dye concentration varied from 10 to 20 ppm, the Photodegradation rate also elevated because more active spots were available on the photocatalyst surface. However, an adverse effect on the rate of

deterioration was observed when the dosage of RG 5 surpassed 20 parts per million. The observed effect might result from adding more RG 5 dye molecules, which could adhere to the photo catalyst's surface and occupy their active positions when the dye dosage is raised. This led to fewer hydroxyl radicals at the photocatalyst surface [20]. Thus, a reaction between H_2O_2 & photocatalyst was cessation, which decreased the degradation rate of RG 5.

Effect of contact time

It is recognized that one of the crucial determinants of photocatalytic degradation processes is the irradiation period. The effect of illumination duration on RG 5 removal by GCN, PPy@GCN and ternary composites is shown in Fig. 11(E). The findings demonstrate that the rate of dye exemption correlates significantly with the contact time, indicating that photodegradation is enhanced as irradiation time increases. A fast increase in dye degradation was observed in the first 60 min of reaction duration, after which the degradation rate decreased and reached a maximum at 120 min. Because there are a lot of hydroxyl radicals accessible in the initial phases, the rate of degradation increases [50]. The reaction continued more slowly as hydroxyl radicals were absorbed over time by the electron-hole pair. Ultimately, this enhances the probability of contact between the RG 5 molecule and electron-hole pairs.

Radical trapping experiments

The mechanism of photocatalytic degradation comprises reactive species, specifically OH radicals, h^+, and e^- [51]. Therefore, to identify the predominant radicals leading to photocatalysis, a radical scavenging experiment was conducted [52]. The 5 m*M* solutions for each of the scavengers DMSO (dimethyl sulfoxide) for scavenging hydroxyl radicals, EDTA (ethylenediamine tetra-acetate) for scavenging holes, and $K_2Cr_2O_7$ (potassium dichromate) for electron scavenging were employed in this study, along with parameters for optimum pH, composite dosage, oxidant quantity, and reaction duration. The results clearly show in Fig. 11(F) that incorporating DMSO lowers the degradation efficacy from approximately 96 % to 25 %. This suggests that hydroxyl radicals played a crucial role in the mechanism of photocatalytic degradation. $K_2Cr_2O_7$ decreases process efficacy from about 94 % to 84 %, whereas EDTA decreases process efficacy from approximately 94 % to 59 %. The outcomes assist the substantial involvement of holes and the lesser involvement of electrons in the RG 5 degradation pathway.

Effect of oxidant dose

The concentration of H_2O_2 was modified from 5 to 20 mM in 50 ml of RG 5 dye solution, both with and without a catalyst, under optimum pH and composite dosage conditions, to examine the effect of oxidant dosage on the percentage degradation of RG 5, as shown in Fig. 12 (A, B). A significant rise in the degradation of dyes through oxidative photocatalysis was observed, along with a considerable increase in hydrogen peroxide levels [48]. The results indicate that a hydrogen peroxide concentration of 10 m*M* was determined to be optimal and that any higher concentration of oxidant harmed the degradation of the dye (Fig. 12 (A)). The catalyst greatly improved the degradation performance, reaching 94 % under ideal conditions, 10 m*M* of H_2O_2, while degradation without a catalyst only resulted in 26 %, demonstrating a considerable catalytic impact, as shown in (Fig. 12 (B)). The addition of a catalyst led to a 3.5-fold improvement in degradation efficiency, highlighting its effectiveness in improving the degradation process and emphasizing its potential for further applications. The operational process of hydrogen peroxide is based on a well-regarded reaction pathway used in the breakdown of dyes, characterized by the swift generation of hydroxyl radicals [49]. The electron is evacuated from the conduction region, contributing to in-charge absorption (Eqs. 7 & 8).

$$H_2O_2 + O_{2^-} \rightarrow HO^{\cdot} + OH^- + O_2 \quad (7)$$

$$H_2O_2 + e^-_{(CB)} \rightarrow HO^{\cdot} + OH^- \quad (8)$$

The formation of the hydrogen peroxide radical caused this phenomenon. According to Eqs. 9 and 10, these radicals perform as HO predators and are less reactive than HO radicals.

$$H_2O_2 + hydroxyl\ radicals \rightarrow water + HO^{\cdot}{}_2 \quad (9)$$

$$HO^{\cdot}{}_2 + HO^- \rightarrow H_2O + O_2 \quad (10)$$

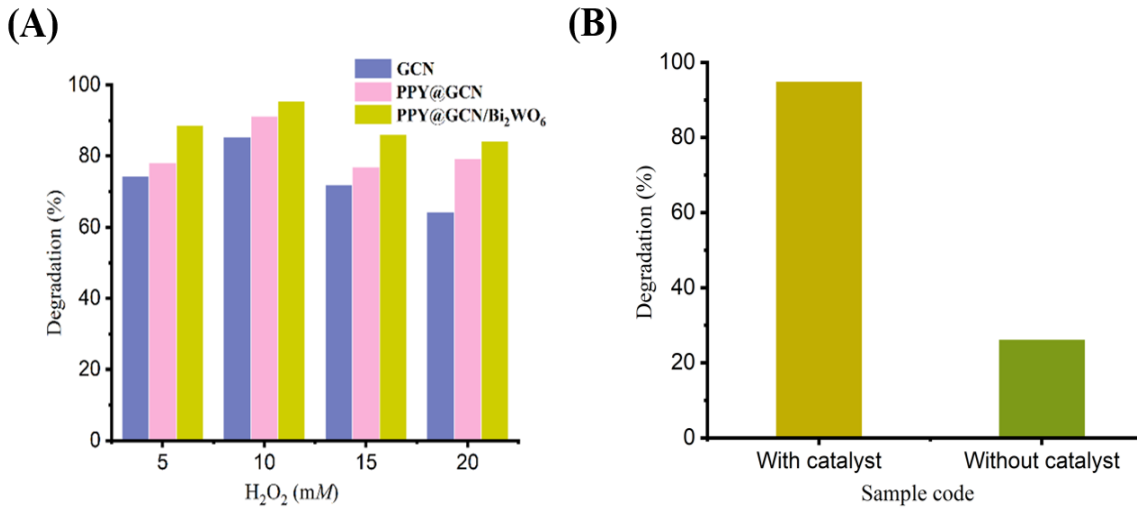

Fig. 12: Effects of oxidant dose on RG 5 dye degradation (A) presence of catalyst, (B) comparison without catalyst.

Kinetic modeling

The kinetic attributes of the various approaches and their analogous coefficients of determination (R^2) values to describe the breakdown of RG 5 dye by the photocatalytic oxidative process within distinct operating conditions were calculated using the algorithm developed for the Behnajady-Modirshahla-Ghanbery (BMG) [53], pseudo 1st order (PFO) [54], and pseudo 2nd (PSO) order kinetic models [55]. The reaction rate coefficients illustrating the heterogeneous photocatalytic decolorization of RG 5 dye by GCN, PPY@GCN, and PGB composites were determined through linear regression and the optimization of different kinetic models. In consequence, the reaction order was assessed by the extent of fit, which was considered through identified (R^2) values. The significant correlation between the data obtained from kinetic models and the experimental findings is achieved when the R^2 values approaches to 1. The breakdown of organic contaminants in aqueous media through AOPS) is typically described by Eq. (11).

$$\frac{d_c}{d_t} = kiC^n \qquad (11)$$

where n = is the order of the reaction, the integer t = is the duration, K_i = is the rate of reaction, and C = is the target pollutant concentration. For first-order processes, this variable has a value of 1. After the integration, Eq. (11) takes the form of Eq. (12).

$$Ct = Co\, e^{k1t} \qquad (12)$$

$$ln[C_t] = ln[C_o] - K_1 t \qquad (13)$$

The Eq. (13) can be rewritten as,

$$\ln \frac{C_o}{C_t} = K_1\, t \qquad (14)$$

The PFO model is represented linearly in this way, t indicates the response time, k_1 for the PFO rate constant, and C_o and C_t denote RG 5 concentrations at integer t = 0 and t = t, respectively. Fig. 13 (A) regarding $ln\,(\frac{C_o}{C_t})$ versus time yields a slope equal to the PFO rate coefficient (K_1).

Pseudo 2nd order kinetic model

For second-order kinetic processes the value of n is 2.

$$\frac{1}{C_t} = \frac{1}{C_o} + K_2 t \qquad 15$$

Consequently, Eq. (15) becomes Eq. (16) upon integration.

$$\frac{1}{C_t} = \frac{1}{C_o} + K_2 t \qquad (16)$$

Where t is the duration, K_2 indicates the PSO kinetics rate constants, 1/Co is the starting RG5 concentration, and 1/Ct is the RG5 concentration after treatment. The plot of 1/Ct vs. time is shown in Fig.13 (B), and the graph's slope determines the value of the PSO rate constant.

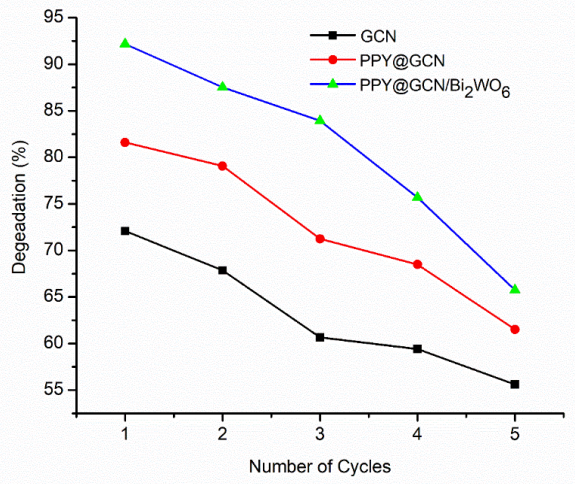

Fig. 13: Kinetic outcomes for RG 5 dye photocatalytic degradation using GCN, PPY@GCN and PPY@GCN/Bi_2WO_6, (A) pseudo 1st order, (B) pseudo 2nd order and (C) BMG kinetic models.

Behnajady-Modirshahla-Ghanbery model

BMG reaction kinetics may be used to investigate the rate at which RG 5 dye fades when exposed to oxidation processes. The non-linear behavior of the BMG reaction kinetics is described by Eq. (17).

$$\frac{t}{1-{C_t}/{C_o}} = m + bt \qquad 17$$

In the given equation, t denotes the reaction time, Co and Ct represent the RG 5 dye concentration at preliminary and any duration (t), m and b are distinctive constants that are associated with the kinetics of the reactions and the process's oxidation capacity, m endures the dimensions of (min), and b represents dimensionless quantity. The value of (1/m) indicates the initial value of pollutant removal. As a result, an elevated value of 1/m denotes a quicker first breakdown of pollutants. Moreover, the value 1/b indicates the highest possible pollutant removal percentage, which could be the same as the treatment system's maximum oxidation capacity as the reaction time approaches infinity. The linearization of Eq. (17) leads to Eq. (18).

$$\frac{t}{1-{C_t}/{C_o}} = m + bt \qquad (18)$$

The factor t / (1-C_t/C_o) is plotted against time in Fig. 13 (C), showing a straight line with intercept values of m and a slope of b. The corresponding degradation rate constants and the coefficient of determination (R^2) indicate that the photocatalytic removal of RG 5 under optimal conditions is illustrated in Table 1. Following the PFO kinetic approach shown in Fig. 13 (A), the intended R^2 values for GCN, PPY @ GCN, and PGB composites are 0.68, 0.64, and 0.83, respectively, indicating that these R^2 values are low compared to one, suggesting that the PFO kinetic model did not fit the experimental data well. However, the PSO kinetic model, as illustrated in Fig. 13 (B), was also unable to adequately characterize the RG 5 dye degradation kinetics for GCN, PPY @ GCN, and PGB composites, with low R^2 values of 0.66, 0.46, and 0.47. However, R^2 values of 0.98, 0.99, and 0.99 were observed in Fig. 13 (C) for the kinetic outcomes from the degradation of RG 5 using the (BMG) model for GCN, PPY @ GCN, and PGB composites, respectively. Thus, the proximity of the RG 5 dye R^2 values to one suggests that the BMG kinetic model strongly agrees with the experimental findings. The numerals in Table 1 indicate the (1/m) and (1/b) data for GCN, PPY @ GCN, and PGB composites. The (1/m) value for the PGB composite is higher than that of pristine GCN and PPY@GCN composites. This demonstrates that the initial RG 5 degradation rate was enhanced with an increased dosage of catalysts, with the PPY@GCN composite performing better, although the PGB composites were significantly quicker. The (1/b) value for both the pristine material and the polymer-treated composite was approximately 1, indicating that the polymer-modified composite effectively facilitated photocatalytic reactions with greater oxidation capabilities. Contributing factors to this trend include the loading of PPY on the GCN/Bi_2WO_6 surface, which lowers the rate of agglomeration, and the formation of an intermediate phase between the VB and CB, which inhibits the recombination rates of the excited exciton.

Reusability

From an economic and ecological perspective, assessing the stability and recyclability of

a photocatalyst is essential [56]. After the degradation process was finished, the composites were revitalized by rinsing the magnet bar three times with deionized water and then drying it in an oven at 60 °C for use in the next cycle. Under optimal conditions, a reusability process is conducted for all prepared composites, specifically at pH 3, with a composite quantity of 10 mg, a contact duration of 60 minutes, an oxidant concentration of 10 m*M*, and a dye concentration of 20 ppm for GCN and its composites. In Fig. 14, the photocatalyst can be employed up to five times while retaining 92 % of its photocatalytic activity with negligible loss in product yield. The results indicated that the PGB composite exhibits improved reusability and mechanical stability.

Table-1: Kinetic study for degradation of RG 5 dye via GCN, PPY@GCN and PGB under visible light irradiation.

Kinetics parameter	GCN	PPY@GCN	PPY@GCN/Bi_2WO_6
Pseudo-1st order			
K1 (min^{-1})	**0.009**	**0.014**	**0.022**
R^2	**0.68**	**0.64**	**0.83**
Pseudo-2nd order			
K2 (min^{-1})	**0.0012**	**0.0017**	**0.0049**
R^2	**0.66**	**0.46**	**0.47**
BMG Kinetic model			
m (min)	**1.27**	**2.06**	**7.53**
b	**1.40**	**1.22**	**1.00**
R^2	**0.98**	**0.99**	**0.99**

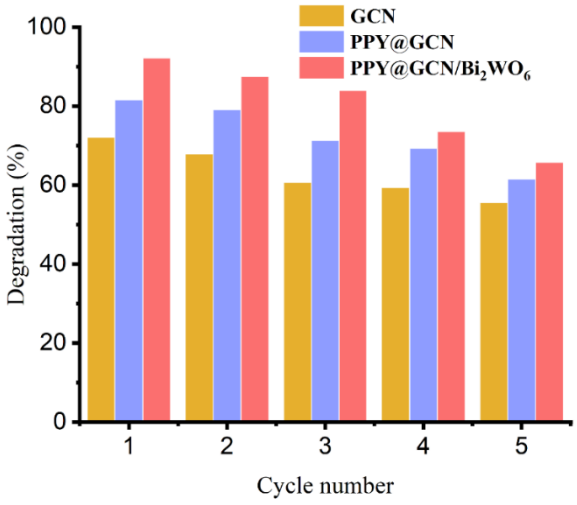

Fig. 14: Stability study capable of 5 reusability runs.

Mineralization study of RG 5

To identify the intermediate substances and evaluate the efficacy of the photocatalytic degradation process, the RG 5 dye solution underwent further examination using FTIR and UV-visible spectroscopy, with the outcomes illustrated in Fig. 15. Pristine RG 5 exhibited distinct peaks at 1579 and 1559 cm^{-1}, as shown in Fig. 15 A (a). These peaks arise from the resonance of the (-C = C-) stretching associated with the aromatic components in the model dyes. The peaks at 1340 and 1315 cm^{-1} correspond to the stretching vibrations of aromatic tertiary amines (–C–N–). The bands detected around 3305 and 3307 cm^{-1} suggest the existence of moisture, highlighting the hygroscopic properties of the model dye. In RG 5, the stretching vibrational phase of azo-specific categories (–N = N–) was observed at approximately 1446 and 1451 cm^{-1}. The moisture level on the KBr disc may have contributed to the intensified –OH band seen in the aqueous RG 5 solution, as shown in Fig. 15 A (b). The presence of the -NH category linked to intermediates with hydroxylated and -NH_2 (amines) groups was confirmed by the splitting of the -OH stretching vibrations at 3300 cm^{-1} following partial RG 5 degradation, as illustrated in Fig. 15 A (c). Most of the peaks decreased significantly at the maximum level of photodegradation of the RG 5 solution, depicted in Fig. 15 A (d), leading to the presence of only wide bands at 3293 cm^{-1} (–OH stretching vibrations) and 1638 cm^{-1} (H–O–H stretching vibrations), likely related to the aqueous medium. Degradation of RG 5 is also marked by a reduction in absorbance intensity at lambda max 660 nm within the UV-visible spectrum, reflecting the breakdown of the chromophore. Before degradation, shown in Fig. 15 B, the dye displays a prominent peak at 660 nm, but the diminished intensity in Fig. 15 C indicates the decomposition of the dye and loss of structural conjugation. This is attributed to initial hydroxylation and partial deamination of RG 5 molecules. Intermediates such as hydroxylated molecules and amine derivatives, particularly partially deaminated products and hydroxylated aromatic structures, are generated. Consequently, continued oxidation results in the breaking of rings, yielding simpler structures and acidic compounds like butenic acid, acetic acid, and acrylic acid. Ultimately, these compounds transform into CO_2, H_2O, or other inorganic minerals. The findings suggest that the degradation process is highly efficient in breaking down aromatic amine structures into smaller fragments, thereby validating the involvement of amine transformations and $^{\bullet}OH$ radicals in the photodegradation process. The degradation products from this process are safe for the environment, indicating that the photocatalytic process does not generate any harmful substances.

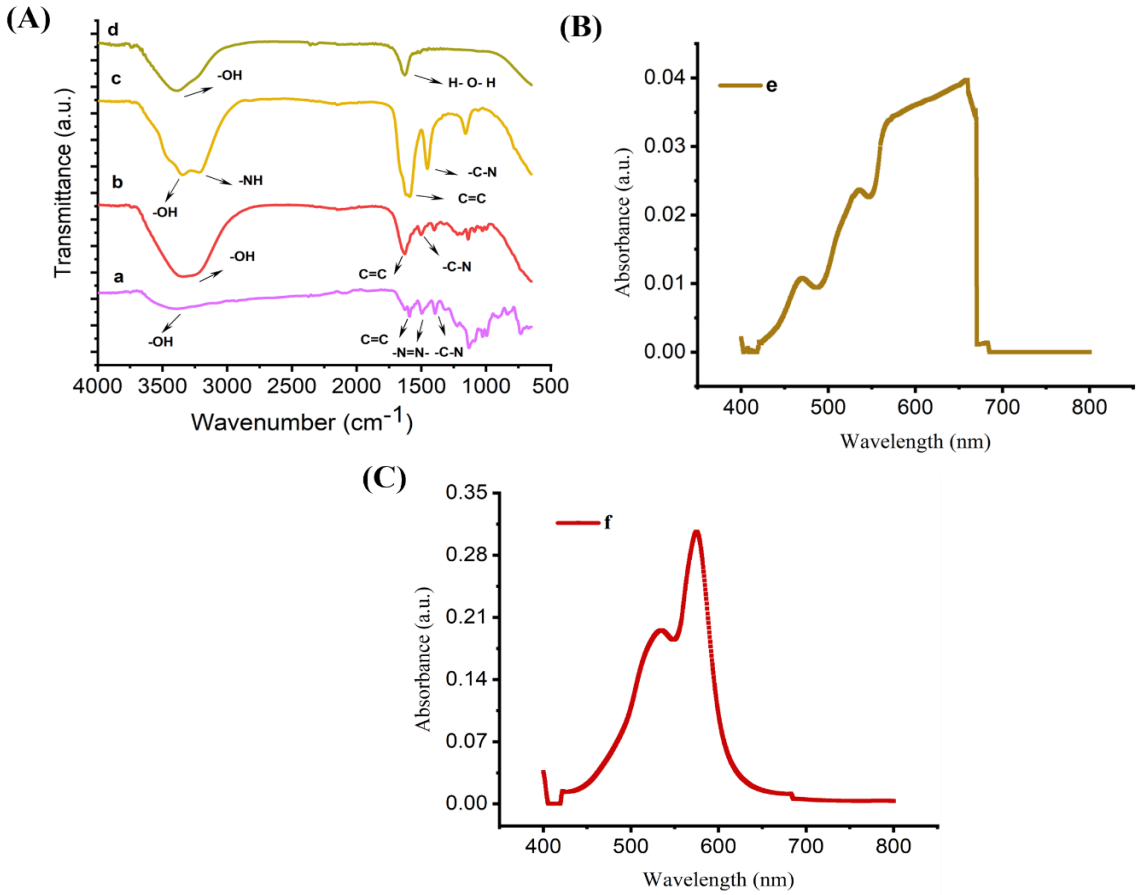

Fig. 15: (A) FTIR outcomes of (a) native RG 5, (b) before degradation, (c) during partial degradation, and (d) after comprehensive degradation, (B) UV-visible spectra of RG 5 solution before degradation (C) After degradation by the PPY@GCN/Bi_2WO_6 composite at pH 3.

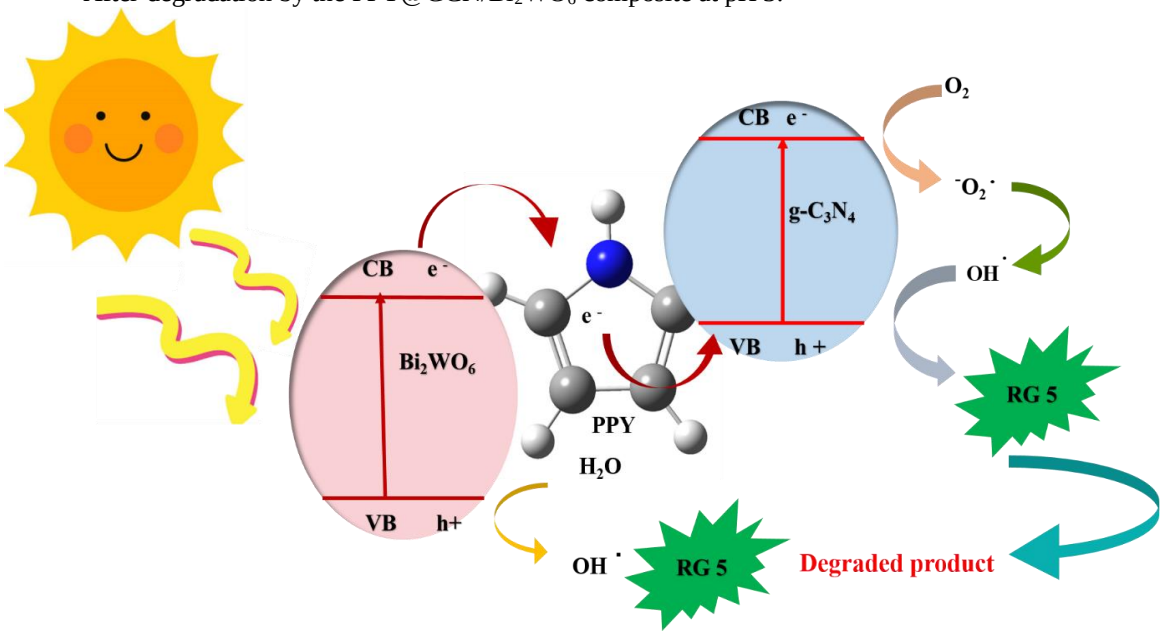

Fig. 16: The feasible photodegradation pathway of PGB composite.

Table-2: Comparison Table of GCN-based composites.

Photocatalyst	Preparation Method	Light source	Contact time	Model pollutants	Degradation (%)	References
$Bi_2WO_6/g\text{-}C_3N_4$	Hydrothermal	Vis	120 min	Ceftriaxone sodium	94.5%	[27]
$g\text{-}C_3N_4/Ag/Zn$	Precipitation	Vis	30 min	Rhodamine B	99 %	[25]
$g\text{-}C_3N_4/Ag@CoWO_4$	Hydrothermal	Vis	120 min	Rhodamine B	97%	[21]
$BWO/g\text{-}C_3N_4$	Hydrothermal	Vis	90 min	Ibuprofen	94.80%	[35]
$NZVI@BiFeO_3/g\text{-}C_3N_4$	Hydrothermal	Vis	120 min	Rhodamine B	97 %	[37]
$g\text{-}C_3N_4$	Thermal- polymerization	Vis	60 min	RG 5	76 %	Present work
PPY@GCN	Situ- Oxidation polymerization	Vis	60 min	RG 5	84 %	Present work
$PPY@GCN/Bi_2WO_6$	Hydrothermal Method	Vis	60 min	RG 5	94 %	Present work

Proposed mechanism for degradation

The suggested photocatalytic mechanism for the PGB composite when exposed to sunlight is illustrated in Fig. 16. Both BWO and GCN are triggered by direct sunlight, and photo-induced electrons from BWO CB move by PPY, an electron mediator, to the GCN VB, integrating segregation through the VB holes of BWO and the CB electrons of GCN. The photo-induced holes in VB of BWO are ingested across H_2O to form •OH radicals. Furthermore, electrons excited by light in the conduction band of GCN are captured by dissolved oxygen, resulting in the formation of the $\bullet O_2^-$ radical anion [57]. Consequently, the hydroxyl radical that forms when the O_2^- anion combines with H_2O_2 efficiently ruptures the RG 5 dye. Following a series of reactions, RG 5 ultimately degraded into non-harmful products like carbon dioxide, H_2O, and assured inorganic ions. As a result, it suggests using the PGB composite, which has greater charge separation efficiency, prolonged charge carrier lifespans, and promising photocatalytic activity. More specifically, PPY may inhibit the passage of electrons retrograde into BWO and enable their migration from BWO to GCN. Consequently, introducing PPY as an adequate support electron facilitator and enhanced mechanical strength to the GCN/BWO composite attributed to a substantial enhancement in photoactivity. Table 2 compares the previously reported GCN-based binary composite.

Conclusion

The GCN heterojunction with BWO and PPY as an endorsed electron-mediated system is presented for the first time in this study. When exposed to solar light, the ternary PGB composite was identified as an effective photocatalyst for environmental remediation. The PGB composite was successfully formed using an in situ hydrothermal method and thoroughly characterized through various analyses, including SEM/EDX, XRD, FT-IR, UV/Vis spectroscopy, antibacterial testing, and PL. The photodegradation of RG 5 in sunlight was studied using the PGB composite. The PGB composite showed a 95 % improvement in the photodegradation of RG 5 in sunlight compared to pristine GCN and PPY@GCN. This was achieved under optimal conditions: pH 3, a composite dosage of 10 mg, a dye concentration of 20 ppm, and an H_2O_2 dosage of 10 m*M*, all within 1 hour. Additionally, the attractive characteristics of PGB include simple synthesis, excellent photocatalytic capabilities, mechanical strength, and remarkable durability. The PGB composite formed in this research presents a novel approach to enhancing the recyclability and photocatalytic efficiency of GCN-based materials.

Acknowledgements

The authors gratefully acknowledge financial support from the University of Agriculture, Faisalabad, Pakistan, to carry out this study.

References

1. S. Zhang *et al.*, Recent developments in fabrication and structure regulation of visible-light-driven $g\text{-}C_3N_4$-based photocatalysts towards water purification: a critical review, *Catal. Today.*, **335**, 65–77 (2019).
2. A. Khan *et al.*, Na-alginate, polyaniline and polypyrrole composites with cellulosic biomass for the adsorptive removal of herbicide: Kinetics, equilibrium and thermodynamic studies, *Arab. J. Chem.*, **16**, 104399 (2023).
3. M. Iqbal *et al.*, Graphene oxide nanocomposite with CuSe and photocatalytic removal of methyl green dye under visible light irradiation, *Diam. Relat. Mater.*, **113**, 108254 (2021).
4. N. M. Hosny, I. Gomaa, M. G. Elmahgary, and M. A. Ibrahim, ZnO doped C: Facile synthesis, characterization and photocatalytic degradation of dyes, *Sci. Rep.*, **13**, 14173 (2023).
5. M. Lal, P. Sharma, L. Singh, and C. Ram,

Photocatalytic degradation of hazardous Rhodamine B dye using sol-gel mediated ultrasonic hydrothermal synthesized of ZnO nanoparticles, *Results Eng.*, **17**, 100890 (2023).
6. H. Alzain, V. Kalimugogo, K. Hussein, and M. Karkadan, A review of environmental impact of azo dyes, *Int. J. Res. Rev.*, **10**, 64–689 (2023).
7. A. Negash, D. Tibebe, M. Mulugeta, and Y. Kassa, A study of basic and reactive dyes removal from synthetic and industrial wastewater by electrocoagulation process," *South African J. Chem. Eng.*, **46**, 122–131 (2023).
8. R. Yavaşer and A. A. Karagözler, Reactive green 5–decorated polyacrylamide/chitosan cryogel: An affinity matrix for catalase, *Appl. Biochem. Biotechnol.*, **192**, 1191–1206 (2020).
9. A. Mittal, R. Jain, J. Mittal, S. Varshney, and S. Sikarwar, Removal of Yellow ME 7 GL from industrial effluent using electrochemical and adsorption techniques, *Int. J. Environ. Pollut.*, **43**, 308–323 (2010).
10. J. Mittal, Permissible synthetic food dyes in India, *Resonance*, **25**, 567–577 (2020).
11. A. Mital and L. Kurup, Column Operations for the Removal and Recovery of a hazardous DyeAcid Red-27'from Aqueous Solutions, Using Waste Materials-Bottom Ash and De-oiled Soya, *Ecol. Environ. Conserv.*, **12**, 181 (2006).
12. A. Khadir, M. Negarestani, and H. Ghiasinejad, Low-cost sisal fibers/polypyrrole/polyaniline biosorbent for sequestration of reactive orange 5 from aqueous solutions, *J. Environ. Chem. Eng.*, **8**, 103956 (2020).
13. U. Chadha *et al.*, A review of the function of using carbon nanomaterials in membrane filtration for contaminant removal from wastewater, *Mater. Res. Express.*, **9**, 12003 (2022).
14. H. N. Bhatti, A. Khan, and U. Kamran, Vachellia nilotica sawdust-derived polymeric and magnetic biocomposites for phosphate ions removal: Kinetics, isothermal, and thermodynamic studies, *Mater. Chem. Phys.*, **326**, 129812 (2024).
15. C. Chinnasamy, N. Perumal, S. Selvaraj, B. B. Pamula, and R. Perumalsamy, Developing environmental purity: Fabricated direct Z-scheme charge transfer in $CuMn_2O_4$/GO heterostructure for superior photocatalytic organic pollutant degradation and electrochemical HER evolution, *J. Water Process Eng.*, **65**, 105701 (2024).
16. M. Iqbal, M. A. Rashid, R. Fatima, M. Iqbal, and H. N. Bhatti, Exploring the impact of cold plasma-induced surface oxygen vacancies on charge carrier dynamics in Z-scheme $CoMoO_6/ZrO_2$/GO heterojunction for efficiency improvement in photocatalysis, *J. Water Process Eng.*, **71**, 107227 (2025).
17. M. Osanloo, F. Khorasheh, and A. Larimi, Development of a novel Z-scheme $TiO_2/CuBi_2O_4$@ GO with enhanced performance for the photocatalytic degradation of metronidazole, *J. Water Process Eng.*, vol. **72**, 107641 (2025).
18. M. J. Molaei, Graphitic carbon nitride (g-C_3N_4) synthesis and heterostructures, principles, mechanisms, and recent advances: A critical review, *Int. J. Hydrogen Energy*, **48**, 32708–32728 (2023).
19. R. Huang, J. Wu, M. Zhang, B. Liu, Z. Zheng, and D. Luo, Strategies to enhance photocatalytic activity of graphite carbon nitride-based photocatalysts, *Mater. Des.*, **210**, 110040 (2021).
20. S. Tahir, M. Zahid, M. A. Hanif, and M. Y. Javed, g-C_3N_4/graphene oxide/$SnFe_2O_4$ ternary composite for the effective sunlight-driven photocatalytic degradation of methylene blue, *Environ. Sci. Pollut.* **30**, 125540–125558 (2023).
21. H. Ashiq *et al.*, G-C_3N_4/Ag@ $CoWO_4$: A novel sunlight active ternary nanocomposite for potential photocatalytic degradation of rhodamine B dye, *J. Phys. Chem. Solids*, **161**, 110437 (2022).
22. Y. Liu, Y. Ma, D. Weng, X. Wu, and Z. Si, Pt@ g-C_3N_4/CeO_2 photocatalyst for the remediation of low concentration NOx at room temperature, *Prog. Nat. Sci. Mater. Int.*, **30**, 308–311 (2020).
23. U. Bharagav *et al.*, Bifunctional g-C_3N_4/carbon nanotubes/WO_3 ternary nanohybrids for photocatalytic energy and environmental applications, *Chemosphere*, **311**,137030 (2023).
24. Y. Lun *et al.*, Highly enhanced photocatalytic property dominantly owing to the synergic effects of much negative Ecb and S-scheme heterojunctions in composite g-C_3N_4/Mo-doped WO_3, *Colloids Surfaces A Physicochem. Eng. Asp.*, **642**, 128682 (2022).
25. P. P. Gotipamul, G. Vattikondala, K. D. Rajan, S. Khanna, M. Rathinam, and S. Chidambaram, Impact of piezoelectric effect on the heterogeneous visible photocatalysis of g-C_3N_4/Ag/ZnO tricomponent, *Chemosphere.*, **287**, 132298 (2022).
26. Y. Zhao *et al.*, Degradation and removal of Ceftriaxone sodium in aquatic environment with Bi_2WO_6/g-C_3N_4 photocatalyst, *J. Colloid Interface Sci.*, **523**, 7–17 (2018).
27. S. A. GokulaKrishnan *et al.*, New insights of g-C_3N_4/Bi_2WO_6 nanocomposite surface assembled on PVDF hybrid membrane for the treatment of pirimicarb pesticides, *J. Taiwan Inst. Chem. Eng.*, 105136 (2023).
28. S. A. GokulaKrishnan *et al.*, New insights of g-C_3N_4/Bi_2WO_6 nanocomposite surface assembled

on PVDF hybrid membrane for the treatment of pirimicarb pesticides, *J. Taiwan Inst. Chem. Eng.*, **166**, 105136 (2025).
29. X. Deng, R. Chen, Z. Zhao, F. Cui, and X. Xu, Graphene oxide-supported graphitic carbon nitride microflowers decorated by sliver nanoparticles for enhanced photocatalytic degradation of dimethoate via addition of sulfite: Mechanism and toxicity evolution, *Chem. Eng. J.*, **425**,131683 (2021).
30. M. H. A. Rehim, A. A. Badawy, and G. Turky, Electrical properties and heavy ions removal ability of graphitic carbon nitride/polypyrrole composite, *J. Phys. Chem. Solids*, **167**, 110741 (2022).
31. A. Atta, E. Abdeltwab, H. Negm, N. Al-Harbi, M. Rabia, and M. M. Abdelhamied, Characterization and linear/non-linear optical properties of polypyrrole/NiO for optoelectronic devices, *Inorg. Chem. Commun.*, **152**, 110726 (2023).
32. M. H. Shakoor *et al.*, Enhancing the Photocatalytic Degradation of Methylene Blue with Graphene Oxide-Encapsulated g-C_3N_4/ZnO Ternary Composites, *ACS omega.*, **9**, 16187–16195 (2024).
33. S. Ullah, A. Gulnaz, S. Anwar, A. Kamal, and H. Wali, Synthetization and Characterization of Zinc Oxide Nanoparticles by X-Ray Diffractometry (XRD), Fourier Transforms, Infra-Red Spectroscopy (FT-IR), Scanning Electron Microscopy (SEM) and Antibacterial Activity Test, *Am. J. Phys. Sci.*, **2**, 1–25 (2024).
34. D. Jiang, W. Ma, P. Xiao, L. Shao, D. Li, and M. Chen, Enhanced photocatalytic activity of graphitic carbon nitride/carbon nanotube/Bi_2WO_6 ternary Z-scheme heterojunction with carbon nanotube as efficient electron mediator, *J. Colloid Interface Sci.*, **512**, 693–700 (2018).
35. A. O. Oluwole and O. S. Olatunji, Synthesis and characterization of binary bismuth tungstate-graphitic carbon nitride (BWO/g-C_3N_4) heterojunction nanocomposites for efficient photodegradation of ibuprofen in aqueous media, *J. Water Process Eng.*, **54**, 104045 (2023).
36. L. Liu, D. Ma, H. Zheng, X. Li, M. Cheng, and X. Bao, Synthesis and characterization of microporous carbon nitride, *Microporous Mesoporous Mater.*, **110**, 216–222 (2008).
37. M. U. Rahman *et al.*, Solar driven photocatalytic degradation potential of novel graphitic carbon nitride based nano zero-valent iron doped bismuth ferrite ternary composite, *Opt. Mater. (Amst).*, **120**, 111408 (2021).
38. P. S. Kumar, B. Shobana, and P. Prakash, Light harvesting enhancement through band structure engineering in graphite carbon nitride/polydopamine nanocomposite photocatalyst: Addressing persistent organophosphorus pesticide pollution in water systems, *Chemosphere.*, **354**, 141708 (2024).
39. D. Ntemogiannis *et al.*, ZnO matrices as a platform for tunable localized surface plasmon resonances of silver nanoparticles, *Coatings*, **14**, 69 (2024).
40. R. M. A. Iqbal *et al.*, Development of Ag0. 04ZrO_2/rGO heterojunction, as an efficient visible light photocatalyst for degradation of methyl orange, *Sci. Rep.*, **12**, 12308, (2022).
41. N. Shaheen *et al.*, Carbon coated tungsten doped molybdenum oxide nanowires and their composite with graphitic carbon nitride for photocatalysis and antibacterial studies, *Ceram. Int.*, **49**, 6906–6922 (2023).
42. L. Bouaziz, M. Dubus, K. Si-Ahmed, H. Kerdjoudj, M. Özacar, and Y. Bessekhouad, Effectiveness of I-doped ZnO as polyvalent material for both anti-bacterial and photocatalytic treatments, *J. Mol. Struct.*, **1255**, 132391 (2022).
43. S. Ahmad *et al.*, Sol-gel synthesis of nanostructured ZnO/$SrZnO_2$ with boosted antibacterial and photocatalytic activity, *Ceram. Int.*, **48**, 2394–2405 (2022).
44. H. A. Alburaih *et al.*, Multifunctional Fe and Gd co-doped CeO_2-RGO nanohybrid with excellent solar light mediated crystal violet degradation and bactericidal activity, *Synth. Met.*, **287**, 117093 (2022).
45. I. Ahmad, S. Shukrullah, M. Y. Naz, and H. N. Bhatti, Synergistic effect of doping-induced oxygen vacancies, in-built Tb^{4+}/Tb^{3+} redox centers and heterojunction on the photocatalytic activity of Sm-doped ZnO/Y-doped Tb_2O_3 for H_2 evolution, *Int. J. Hydrogen Energy.*, **48**, 29485–29496 (2023).
46. M. A. Munir, M. Y. Naz, S. Shukrullah, M. T. Ansar, G. Abbas, and M. M. Makhlouf, "Microwave plasma treatment of NiCuZn ferrite nanoparticles: a novel approach of improving opto-physical and magnetic properties, *Appl. Phys. A.*, **128**, 345 (2022).
47. T. A. Jabar and K. M. M. Al-zobai, Removal of Reactive Green Dye from Textile Waste Water by Photo Fenton Process: Modeling, Kinetic, and Thermodynamic., *Al-Nahrain J. Eng. Sci.*, **24**, 104–111 (2021).
48. N. Nadeem *et al.*, Coal fly ash-based copper ferrite nanocomposites as potential heterogeneous photocatalysts for wastewater remediation, *Appl. Surf. Sci.*, **565**, 150542 (2021).
49. S. S. Emmanuel, A. A. Adesibikan, and O. D. Saliu, Phytogenically bioengineered metal nanoarchitecture for degradation of refractory dye

water pollutants: A pragmatic minireview, *Appl. Organomet. Chem.*, **37**, e6946 (2023).

50. P. Zhang, F. Wang, Y. Qin, and N. Wang, Exfoliated graphitic carbon nitride nanosheets/gold nanoparticles/spherical montmorillonite ternary porous heterostructures for the degradation of organic dyes, *ACS Appl. Nano Mater.*, **3**, 7847–7857 (2020).
51. F. Mushtaq *et al.*, $MnFe_2O_4$/coal fly ash nanocomposite: a novel sunlight-active magnetic photocatalyst for dye degradation, *Int. J. Environ. Sci. Technol.*, **17**, 4233–4248 (2020).
52. F. Khan, M. Zahid, H. N. Bhatti, and Y. Jamil, Degradation of persistent organic pollutant using Ag-doped ZnO-ZnS–polyaniline composite as photocatalyst, *Int. J. Environ. Sci. Technol.*, **20**, 4811–4826 (2023).
53. M. A. Behnajady, N. Modirshahla, and F. Ghanbary, A kinetic model for the decolorization of CI Acid Yellow 23 by Fenton process, *J. Hazard. Mater.*, **148**, 98–102 (2007).
54. Y. S. Ho and C. C. Chiang, Sorption studies of acid dye by mixed sorbents, *Adsorption.*, **7**, 139–147 (2001).
55. Y.-S. Ho and G. McKay, Pseudo-second order model for sorption processes, *Process Biochem.*, **34**, 451–465 (1999).
56. M. J. Azizli, E. Vafa, K. Rezaeeparto, S. Parham, M. Mokhtary, and Z. Jahankhah, Preparation, characterization, and compatibilization of novel rubber nanocomposites for mechanical applications: relationship between electrical properties, morphology, and rheology, *J. Adhes. Sci. Technol.*, **37**, 2754- 2778 (2023).
57. W. Sardar *et al.*, Systematically designed g-C_3N_4/rGO/MoS_2 nanocomposite for enhanced photocatalytic performance, *Curr. Appl. Phys.*, **57**, 42–48 (2024).